Desalination and Water Treatment
www.deswater.com

doi: 10.5004/dwt.2022.28250

250 (2022) 298–311
February

Comparative study on concentric cylindrical glass tube microreactor, UV-LED strip photocatalytic reactor and classical annular reactor on Acid Red 87 removal

Kaviya Piriyah Sundar*, S. Kanmani

Centre for Environmental Studies, Department of Civil Engineering, Anna University, Chennai, India, Mobile No.: +91-7299284310; email: kaviya1305@gmail.com (K.P. Sundar), Mobile No.: +91-9444585805; email: skanmani@hotmail.com (S. Kanmani)

Received 17 September 2021; Accepted 21 January 2022

ABSTRACT

The present study is an exhaustive comparison between three types of reactors for Acid Red 87 removal using graphene oxide under combined processes. Acid Red 87 or Eosin Y is brominated fluorescein structure which forms a red fluorescence. From late 19th century, this dye was extensively used in textile industries. The degradation of this fluorescent dye is problematic due to its high molar mass and stability. The performance of three reactor types: (1) concentric cylindrical glass tube microreactor (CGTR), (2) UV-LED strip photocatalytic reactor and (3) classical annular reactor were evaluated for the Acid Red 87 removal. The maximum of 94.8% dye removal and 61.5% total organic carbon removal was achieved at initial pH 6, 2 g/L catalyst dosage and 44 mM H_2O_2 concentration under 60 min in CGTR. Further comparative parameters were calculated and the best parameter values were obtained for CGTR in terms of performance and energy efficiency.

Keywords: Synergistic process effect; UV-LED micro-depth reactor; Comparative study; Photocatalytic reactors

1. Introduction

Discharge from textile industries is one of the major environmental concern, regarding the pollution of water environment. Annually around 15% of 700,000 tons of 100,000 types of dyes produced gets wasted during the production and processing stages [1]. Azo dyes are one of the most extensively used dyes in textile industries, which have many number of research publications [2,3]. Out of all dye degradation studies, only around 1% of works were related to fluorescent dye degradation. Acid Red 87 or Eosin Y is one of the red fluorescent dyes, which comprises of a conjugated Π system. They are used in safety clothing, ink manufacturing and colouring cosmetics. Wastewater containing Acid Red 87 causes serious environmental problems due to its stability and dark colour [4].

Due to the stringent standards on the quality of treated wastewater, removal of these coloured compounds is very important prior to the discharge into environment. Till now various physical, chemical and biological treatment techniques have been carried out for dye removal. In this regard, advanced oxidation processes (AOPs) are very efficient due to the generation of active hydroxyl radicals ($OH^{\bullet}$) which have high oxidative potential. Most of the AOP studies have demonstrated treatments like Fenton oxidation [4], solar photocatalysis [5], H_2O_2 oxidation [6], ultrasonic cavitation [7] and hydrodynamic cavitation [8]. In general, these processes have advantages which includes complete mineralisation and zero end wastes. On the other hand, these processes also has its own limitations such as pH selectivity, longer reaction time, higher dose of chemical oxidant requirement and higher energy requirement

* Corresponding author.

respectively. Coupling of these advanced treatment methods could achieve high performance within short duration of time.

There are various works which demonstrated the coupling of adsorption/photocatalysis/hydrodynamic cavitation/ultrasonification/oxidant addition and ozonation [9–11]. Also recent studies have shown that the use of reactive oxygen species generator such as persulfate/peroxymonosulfate in combination with the photocatalysis/electrochemical process was very efficient in removal of organics [12,13]. The effectiveness of the combined process was accounted using a term synergetic index which was always greater than 1. Thus this implies that combination of advanced oxidation process is a convenient approach in degrading complex dyes or other wastewaters [9].

The well-known photocatalyst TiO_2 is widely used because of its chemical inertness, strong oxidizing power and long-term stability against the light [14]. But the drawback is the rapid recombination rate of photogenerated electron–hole pairs, resulting in low quantum efficiency [15]. On the other hand, graphene alone can act as a good photocatalyst because of its excellent properties including good thermal conductivity of about 3,000–5,000 W/m K, high electron mobility of 15,000 cm^{-2}/Vs, high specific surface area around 2,630 m^2/g and excellent catalytic properties [16]. The band structure is mainly dependent on the relationship between the energy and momentum of electrons. There is a constraint in the movement of electrons in two dimensional surface. Graphene has zero bandgap because the conduction and valence bands meeting at the Dirac points. However when graphene is functionalised with oxygen and hydroxyl groups, this could enhance optical and electronic properties of the graphene oxide. On C–O covalent bonds formation, the two carbon in sub-lattices gets separated by p and p* orbitals creating a bandgap in graphene oxide [17]. The electrons from p valence band gets excited to p* conduction band, creating electron–hole pairs with less recombination effect.

In the performance of photocatalysis, the major influencing factors are light source, photocatalyst material and photocatalytic reactor design. The parameter that plays an important role on the pollutant removal efficiency is design of photocatalytic reactor. Besides the shape of reactor, the other factors such as inlet pipe, liquid pump, hydrodynamic regime (CSTR or PFR), depth of substrate, distance between light source and fluid also contribute to the overall performance efficiency of the photocatalytic process [18]. Even though the use of LEDs could increase the energy efficiency of the photocatalytic reactor, the LEDs orientation and depth of pollutant could not be a trade-off to attain high performance and energy efficiency.

In this study various comparative parameters such as Apparent kinetic constant (k_{app}), space time yield (STY), photocatalytic space time yield (PSTY), specific removal rate (SRR), electrical energy consumption (EEC), mmoles of organic carbon removed/kWh, mmoles of incident photons/kWh and photonic yield [3,19,20,46] were calculated for the performance evaluation of three types of reactors (CGTR, STR, CAR) with same electrical energy input (24 W) and residence time (0.133 min). This work approaches to deliver a novel procedure to quantitatively compare the photocatalytic reactors with 8 comparative parameters. The study concludes that micro-depth reactor could be the best efficient in terms of performance and energy utilisation.

2. Materials and methods

2.1. Chemicals

Acid Red 87 dye (Chemical formula: $C_{20}H_6Br_4Na_2O_5$, Molecular weight: 691.85 g/mol, Absorption maximum: 516 nm) was procured from Sigma-Aldrich. Graphene oxide (thickness 5–20 nm and average particle diameter was 1–10 μm) photocatalyst, was purchased from Nano Wings Pvt. Ltd., India. Sodium hydroxide (NaOH), hydrochloric acid (HCl) and Hydrogen peroxide (H_2O_2) were procured from Thermo Fisher Scientific, United States. These chemicals were used for the pH adjustment in the initial dye solution and peroxide addition to enhance reaction. Distilled water was used to prepare all solutions.

2.2. Catalyst characterisation

The photocatalyst graphene oxide was characterized for particle size. The X-ray diffractogram was recorded on a X'PERT-3 diffractometer system using Cu Kα1 radiation (λ = 0.15406 nm), over the 2θ range 5°–90°. The average crystal size of graphene oxide nanophotocatalysts was calculated using Debye–Scherrer equation [Eq. (1)] with the shape factor K as 0.9 [22].

$$\text{Crystallite size}\left(\text{nm}\right) = K\frac{\lambda}{W\cos\theta} \tag{1}$$

where λ is the wavelength of the X-ray diffraction radiation, W is full width at half maximum (FWHM) in radians, and θ is the Bragg's angle. The morphology and elemental composition was analysed by scanning electron microscopy (SEM) and energy-dispersive X-ray spectroscopy (EDS). The bandgap energy was determined using UV-Visible diffuse reflectance spectra (UV-Vis-DRS) analysis. The UV-Vis-DRS were recorded at room temperature in the wavelength range 200–900 nm on a JASCO V-650 instrument. The bandgap energy was calculated according to following equation [Eq. (2)] [23]:

$$\text{Band gap energy}\left(\text{eV}\right) = \frac{hc}{\lambda} = \frac{1240}{\lambda} \tag{2}$$

where h is Planck's constant (4.1357×10^{-15} eV s), c is the velocity of light (2.998×10^8 m/s) and λ is the wavelength (nm). Fourier-transform infrared spectroscopy (FTIR) spectroscopic studies were carried out using a Perkin-Elmer spectrophotometer. The spectra were recorded in the range 500–4,000 cm^{-1}. The Brunauer–Emmett–Teller (BET) surface area was analysed using Micromeritics ASAP 2020.

2.3. Reactor designs

The three photocatalytic reactors chosen for the study was operated in closed recirculation with the submersible

pump in the reservoir tank of volume throughput of 1 L. The three reactor types are cylindrical glass tube microreactor (CGTR), strip photocatalytic reactor (STR) and classical annular reactor (CAR) with input electrical energy 24 W, but different fluid/substrate depth and fluid-light source distance. The working temperature was 25°C. During the operation, the change in temperature was negligible in CGTR due to high surface area of outer shell, whereas for STR and CAR, the temperature was controlled using a cooling jacket. Even though the capacity of reactors are different, the residence time per fluid pass (Volume/Flow rate) was kept constant in all reactors. The inlet flow rate was controlled using the control valve. The inlet pressure was measured using 0–1 bar pressure gauge. The cavitation number was calculated as per below equation [Eq. (3)] [8].

$$\text{Cavitation number} = \frac{P_{\text{inlet}}}{\rho v^2 / 2} \tag{3}$$

where P_{inlet} is the inlet pressure of fluid, ϱ is density of fluid and v is the inlet velocity of fluid. The effective fluid/substrate depth (F_{eff}) is the longest distance the light travels inside the fluid in order to touch the exterior end of fluid or substrate in orthogonal direction to the fluid flow. The fluid to light source distance (FL) is the shortest distance between light source and outer shell surface (Table 1).

Table 2 presents the dimensions and operating conditions of three reactors.

2.4. Concentric cylindrical glass tube microreactor

The CGTR (Fig. 1) consists of concentric glass tube (micro-gap 2 mm) of length 60 cm and diameter 8 cm which was fitted inside the stainless steel (SS) outer vessel of length 60 cm and diameter 14 cm and appropriate enclosures onto the sides. In the interior walls of outer vessel, 300 numbers of UVA LEDs strip (manufactured by LightingWill) of λ_{max} = 365 nm was disposed circumferentially. The power supply required for UVA LEDs strip was 24 W (80 mW/LED).

2.5. UV-LED strip photocatalytic reactor

The STR (Fig. 2) consists of cylindrical glass tube of length 24 cm and diameter 3 cm which was kept inside the SS

Table 2
Description of reactors

Reactor	CGTR	STR	CAR
Working volume (mL)	300	100	600
Effective fluid substrate (cm) F_{eff}	0.2	3	5.25
Fluid-light source distance (cm) FL	3	5	3
Inlet flow rate (L/min)	2.25	0.75	4.68
Residence time (min)	0.133	0.133	0.133
Inlet pressure (bar)	0.13	0.085	0.2
Cavitation number	0.9	5	0.3

Table 1
Fluid depth and fluid-light source distance

Cross-sectional view of CGTR	Cross-sectional view of STR	Cross-sectional view of CAR
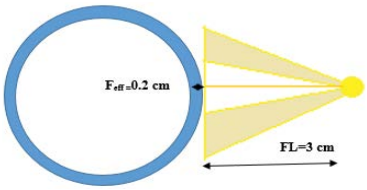	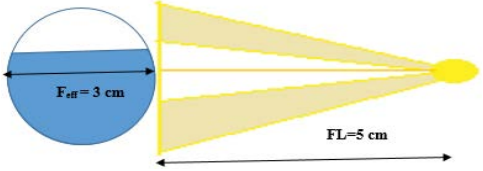	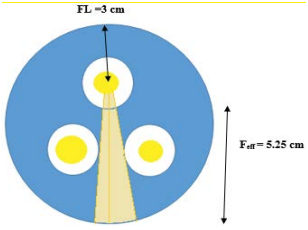

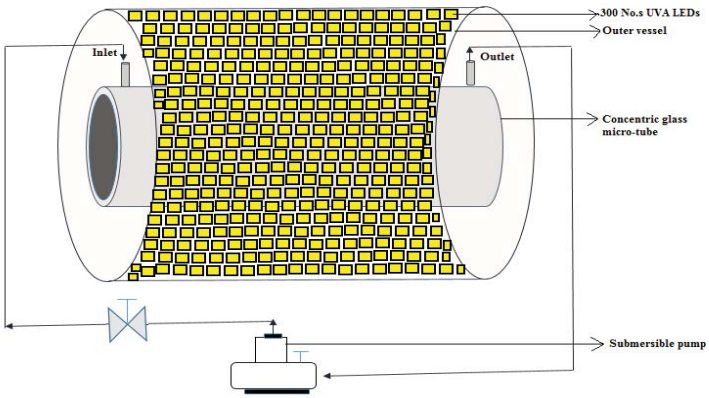

Fig. 1. Schematic representation of the CGTR.

outer cylindrical shell of length 17 cm and diameter 14.5 cm. The UVA LEDs configuration in STR was similar to CGTR.

2.6. Classical annular reactor

The CAR (Fig. 3) consists of SS cylindrical outer vessel of length 14 cm and diameter 10 cm. On the top, there are three apertures wherein the 3 × 8 W PL-lamps (manufactured by Pixnor) of λ_{max} = 365 nm were fitted inside a quartz tube (length 13 cm and diameter 3.5 cm).

2.7. Experimental procedure

The photocatalytic experiments were carried out under optimised conditions (graphene oxide photocatalyst of dosage 2 g/L, initial pH 6 and 44 mM H_2O_2) for maximum dye removal. The 10 ppm of Acid Red 87 dye was the initial dye concentration.

The samples were collected at the outlet of the reactor and analysed for absorbance with the use of UV-Visible spectrophotometer at wavelength 516 nm for every 10 min time interval. The colour removal (%) was calculated using below equation [Eq. (4)]:

$$\text{Colour removal}\left(\%\right) = \frac{A_o - A}{A_o} \tag{4}$$

where A_o and A are the initial absorbance and final absorbance of the solution.

Total organic carbon was estimated using TOC analyser (Shimadzu TOC-L Series) for the calculation of the mmoles

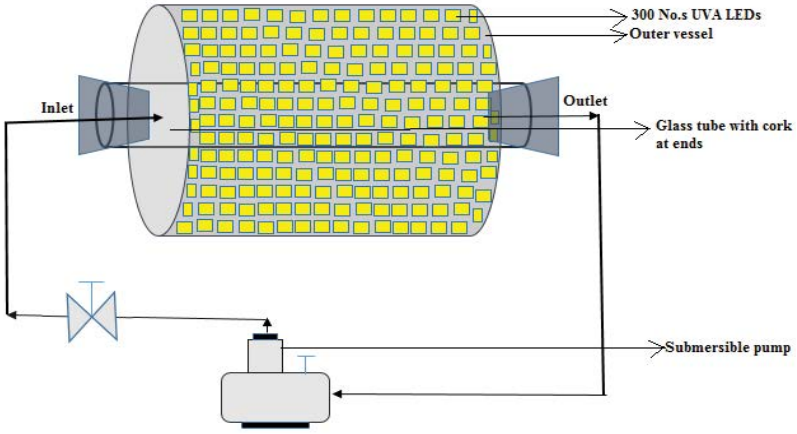

Fig. 2. Schematic representation of the STR.

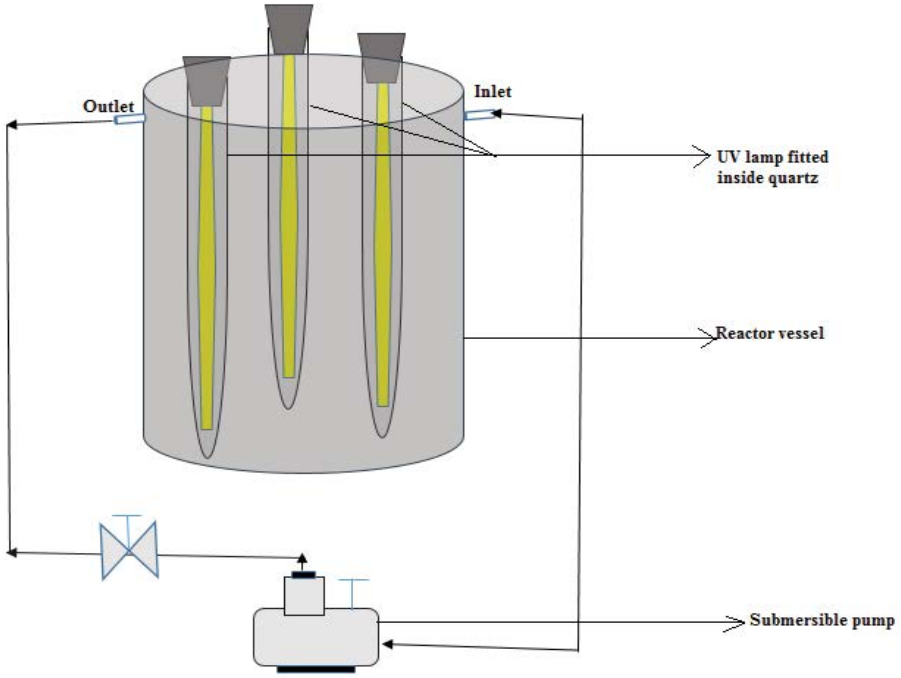

Fig. 3. Schematic representation of the CAR.

of organic carbon removed per kWh. The four experimental conditions were evaluated for the three reactors: photocatalysis under simultaneous adsorption and hydrodynamic cavitation (PCSA+HC), photocatalysis under simultaneous adsorption (PCSA), photocatalysis under initial adsorption and hydrodynamic cavitation (PCIA+HC), photocatalysis under initial adsorption (PCIA). In PCSA, the photocatalyst was suspended simultaneously when the light source was switched on. In PCIA, the photocatalyst was added 30 min prior to photocatalysis, to attain adsorption equilibrium. In PCSA+HC and PCIA+HC, the hydrodynamic cavities were induced by the inlet pressure and reactor inlet constriction.

3. Results and discussions

3.1. Photocatalyst characterisation

The average crystal size of graphene oxide was calculated to be 22.23 nm. The graphene oxide showed broad peak at 2θ = 26.57°, which corresponds to the diffraction line (002) with the intercellular spacing in the crystal 0.3354 nm shown in Fig. 4. The distance between fields in the graphene oxide was due to the presence of oxygen-functional groups and water molecules into the carbon layer structure [24]. The other peaks (004) and (110) were also observed at 2θ = 54.7° (d = 0.1677 nm) and 2θ = 77.7° (d = 0.1228 nm) [25]. Along with the above peaks, peaks at 2θ = 42.63° (d = 0.2120 nm), 44.75° (d = 0.2025 nm) and 83.83° (d = 0.1153 nm) corresponding to planes (100) and (101), and (112) were observed. This indicates that three-dimensional stacking regularity of the carbon layers was maintained in the graphene oxide as in the case of graphite.

The SEM and EDS images of graphene oxide are shown in Fig. 5. The SEM micrographs of graphene oxide showed the formation of flaky sheet like structure [26]. The elemental composition revealed the presence of carbon (59.98%) and oxygen (34.01%). Oxygen functionalization influenced the band gap of graphene oxide. The oxygen/carbon ratio of 50% opened the band gap to 3–3.2 eV [27]. Also when comparison between three types C/O ratio (1.5, 2.1 and 3.5) of GO membranes were previously investigated showed that there was an influence on the proton and electron conductivities by the functional groups. The hydrophilicity of C/O (1.5) resulted in higher water intake than C/O (2.1 and 3.5) which resulted in better conductivity and photocatalytic activity [28].

The FTIR spectrum is shown in Fig. 6. The presence of oxygen containing functional groups in GO was observed

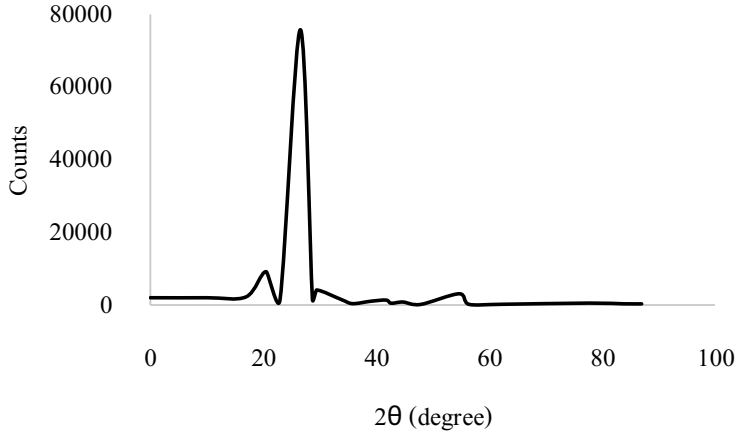

Fig. 4. X-ray diffraction spectra of graphene oxide.

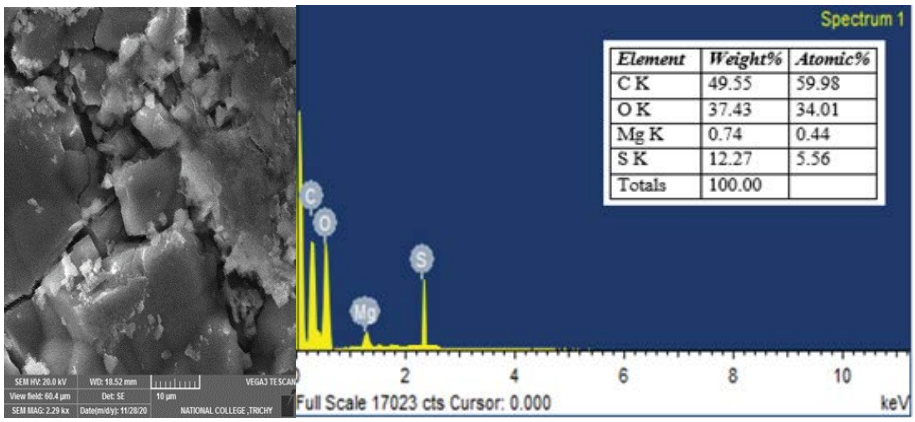

Fig. 5. SEM and EDS of graphene oxide.

in FTIR spectroscopy. The presence of OH groups was confirmed by the broader peaks around 3,200–3,800 cm^{-1}. There was also two broad bands of C=O (carboxyl and carbonyl groups) stretching vibrations from carboxyl and carbonyl groups (1,681.45 and 1,778.70 cm^{-1}). The intensity of O–H bending vibrations was higher due to the presence of more hydroxyl groups (1,396.24 cm^{-1}). Also C–O–C vibrations (1,226.43 cm^{-1}) and C–O (alkoxy) stretching peak at 1,069.47 cm^{-1} were observed [29]. There was no formation of stronger peaks around 1,600–1,620 cm^{-1} corresponding to the absorption bands of C=C skeletal vibrations from unoxidized sp^2 C–C bonds, which indicated that graphite was oxidized to graphene oxide.

The UV-Vis diffuse reflectance absorption spectra of graphene oxide was shown in Fig. 7. The absorbance data with respect to wavelength were used to calculate the modified band gap energies using Kubelka–Munk equation. The band gap of graphene oxide was calculated to be 3 eV respectively. The band gap values were reported the same according to previous literature [30]. The bandgap of the graphene oxide increased with the increase of oxygen coverage density. Graphene is a zero-bandgap material. To widen the bandgap, defect engineering plays an imperative role. In a study of GO bandgap, the increase in O/C ratio from 11% to 50% increased the bandgap from 0.78 eV to 3.2 eV [27]. Therefore the photocatalyst was suitable for activation under UVA irradiation (λ_{max} = 365 nm).

To determine the surface area of graphene oxide, BET analysis was carried out using liquid nitrogen adsorption–desorption isotherms as shown in Fig. 8. The isotherm curve along with pore-size distribution was calculated using the Barrett–Joyner–Halenda (BJH) method [31]. The specific surface area of graphene oxide was 8.68 m^2/g. The pore volume and pore width of graphene oxide was 0.06 cm^3/g and 35 nm respectively.

3.2. Comparison of dye removal

The results of various experimental conditions (1. PCSA+HC, 2. PCSA, 3. PCIA+HC, 4. PCIA, 5. photolysis, 6. HC)

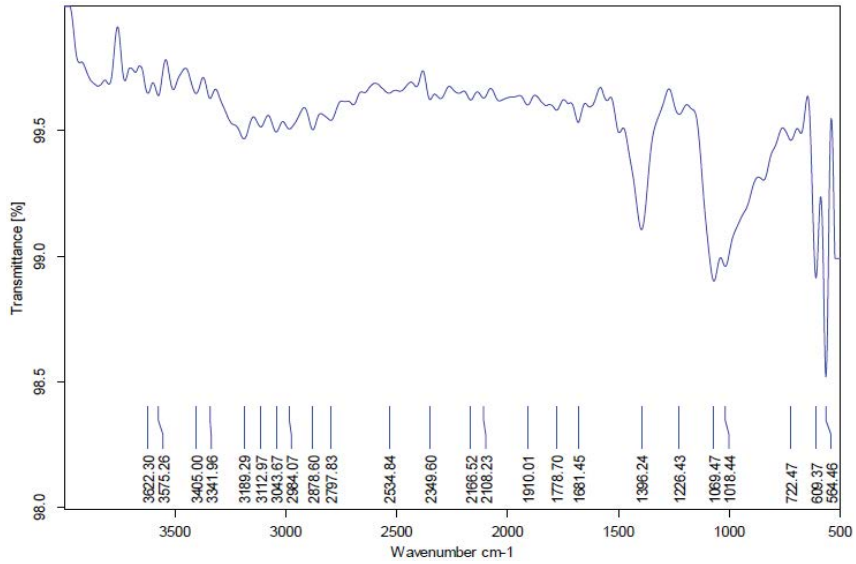

Fig. 6. FTIR spectrum of graphene oxide.

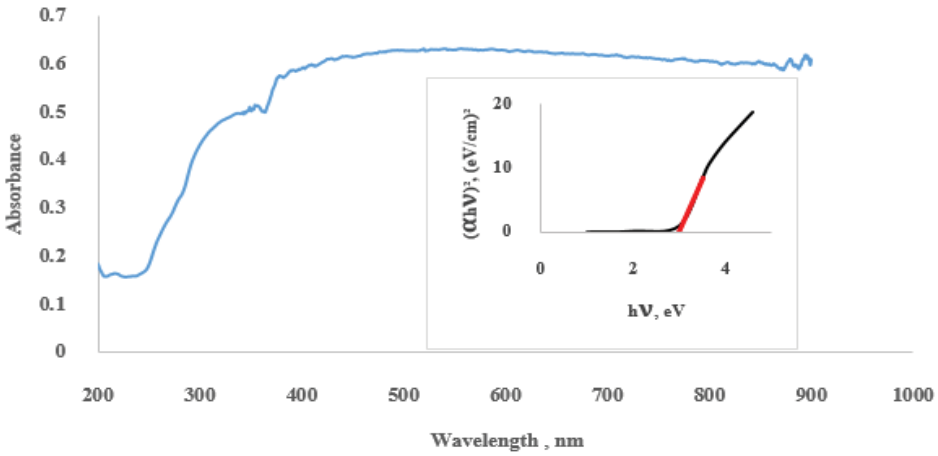

Fig. 7. UV-Vis diffuse reflectance absorbance of graphene oxide.

are illustrated in Fig. 9, which indicated the dye removal % for the three reactors for 10 ppm of Acid Red 87 under optimised conditions. The optimised conditions were initial pH 6, graphene oxide dosage 2 g/L and H_2O_2 44 mM. All the dye removal experiments were repeated thrice to obtain the results with a standard deviation error of <5%.

Among all the experimental conditions, PCSA+HC showed the highest dye removal of 94.8% in CGTR (Fig. 10). The second highest removal (87.4%) was observed in the STR at PCSA+HC. In CAR, 57.1% of dye was removed at PCSA+HC. These results implied that CGTR was the best configuration compared to STR and CAR.

It was observed that PCSA+HC exhibited highest performance in all reactors, due to the increased synergetic effect of photocatalysis, adsorption and hydrodynamic cavitation [11]. In PCSA+HC, there was simultaneous occurrence of two events, that is, affinity of dye molecules towards photocatalyst for adsorption and activation of photocatalyst by photons (Fig. 11a). But in the case of PCIA or PCIA+HC, the photocatalyst and dye attained adsorption equilibrium before the start of irradiation [32]. This is the case where the photocatalyst surface would be saturated with dye molecules, hindering the passage of light photons onto to catalyst surface for activation (Fig. 11b).

The individual processes such as photolysis and hydrodynamic cavitation showed insignificant effect in dye removal. But, there was 17.5% and 30% colour removal at natural pH 8 and initial pH 6 under adsorption at 2 g/L graphene oxide. This may be attributed to the adsorption ability of carbonaceous materials for organic and inorganic molecules [33].

The kinetic constants were derived plotting $-\ln(C/C_o)$ and reaction time for all three reactors for various experimental conditions (Figs. 12–14). The two stage dye removal process was observed at PCSA+HC, consisting of adsorption dominant kinetic constant (K_1) and photocatalysis dominant kinetic constant (K_2). Similarly for PCSA, there was an adsorption dominant kinetic constant (K_1') and

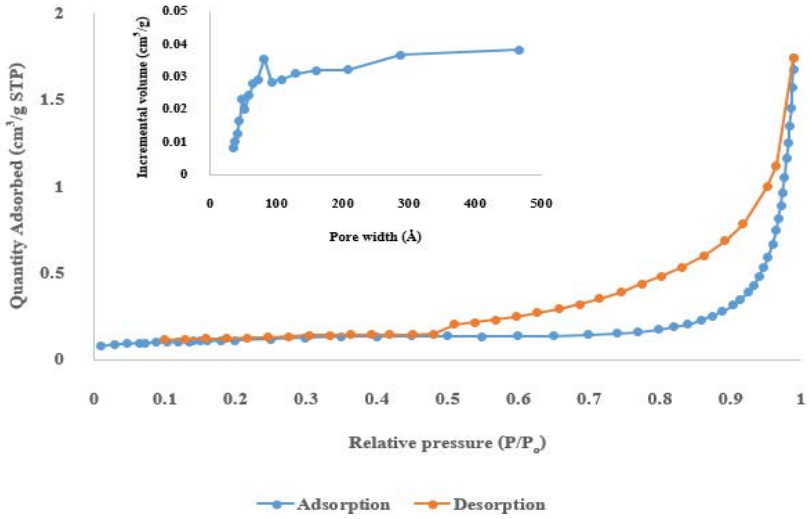

Fig. 8. N_2 gas adsorption–desorption isotherms and pore-size distribution of graphene oxide.

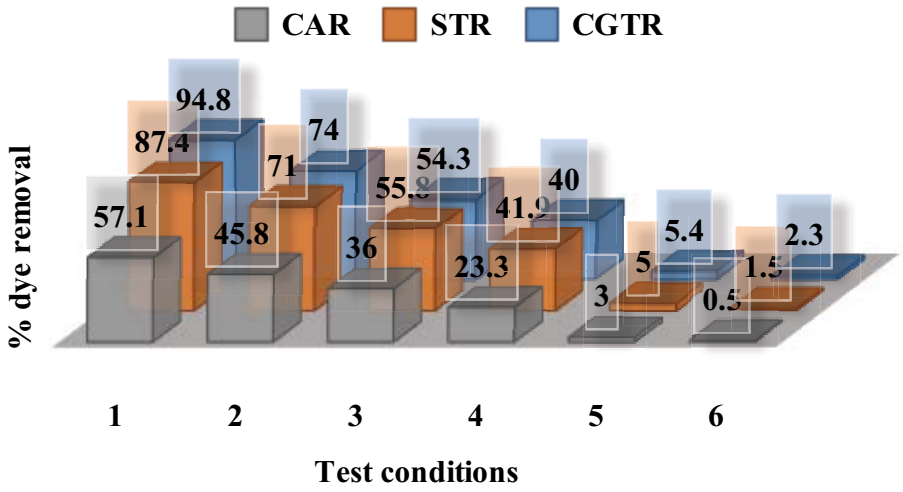

Fig. 9. % dye removal for different experimental conditions (1. PCSA+HC, 2. PCSA, 3. PCIA+HC, 4. PCIA, 5. photolysis, 6. HC).

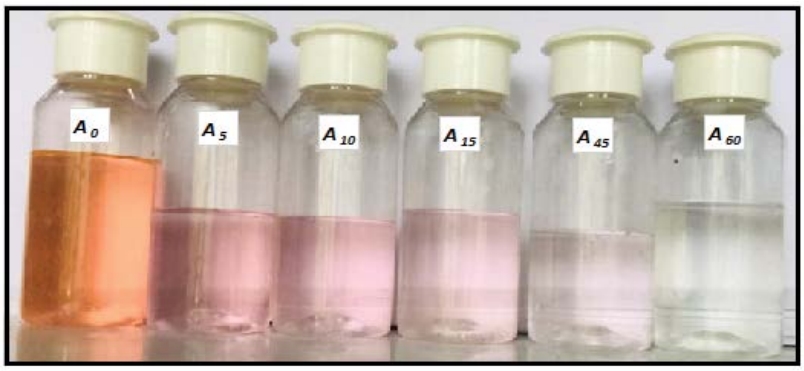

Fig. 10. Acid Red 87 decolourization.

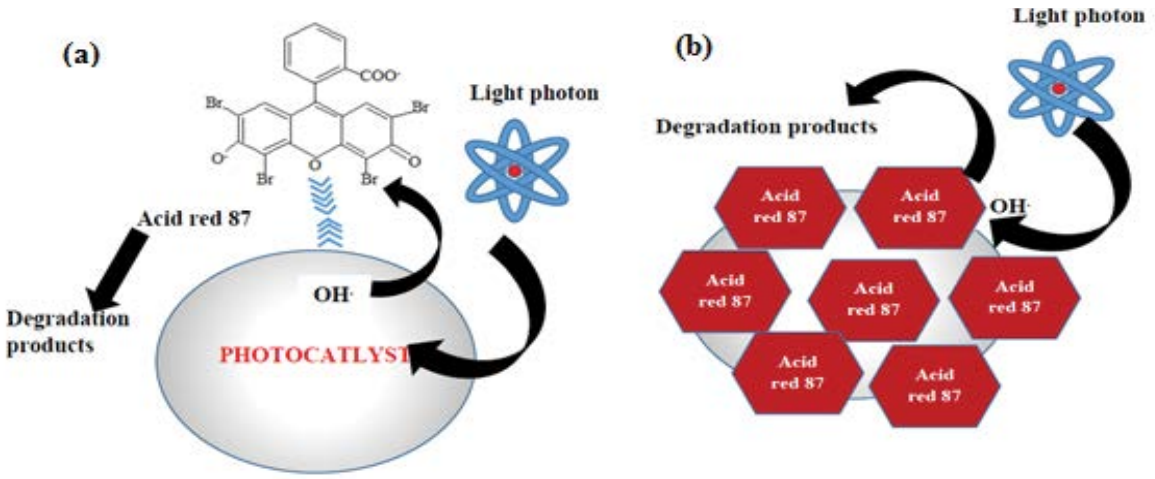

Fig. 11. Schematic representation of (a) PCSA and (b) PCIA.

photocatalysis dominant kinetic constant (K_2'). In the case of PCIA+HC and PCIA, the linearity was observed while plotting $-\ln(C/C_o)$ and t. This implied that the processes followed pseudo-first-order reaction [34].

Generally, Langmuir–Hinshelwood model is used to derive apparent reaction rate constant for heterogeneous photocatalysis. In Langmuir–Hinshelwood, both the reactant species (dye molecules and H_2O) are adsorbed to the catalyst. The rate (r) is influenced by the coverage constant (θ) of both dye molecules and water, expressed as below equations [Eqs. (5)–(7)] [35], where k is fundamental representation of catalyst activity, K_{dye} and K_{water} the adsorption equilibrium constant of the Langmuir isotherm for dye and water respectively.

$$r = k\theta_{dye}\theta_{water} \tag{5}$$

$$\theta_{dye} = \frac{K_{dye}C_{dye}}{1 + K_{dye}C_{dye}} \tag{6}$$

$$\theta_{water} = \frac{K_{water}C_{water}}{1 + K_{water}C_{water}} \tag{7}$$

The H_2O is in higher concentration, coverage constant of water tends to unity, simplifying the rate equation as below [Eq. (8)].

$$r = k\frac{K_{dye}C_{dye}}{1 + K_{dye}C_{dye}} \tag{8}$$

If $C_{dye} < 10^{-3}$M, then denominator tends to unity, further simplifying the equation [Eq. (9)].

$$r = kK_{dye}C_{dye} = K_{app}C_{dye} \tag{9}$$

In the case of PCSA+HC and PCSA, the dye molecules were not stirred under dark, prior to the start of irradiation. Therefore the Langmuir–Hinshelwood model is invalid in this case. Therefore Eley–Rideal model was adopted in this case to derive the apparent reaction rate constant [38]. In Eley–Rideal model, the rate is dependent concentration of dye molecules alone (C_{dye}) [Eq. (10)].

$$r = kC_{dye}\theta_{water} \tag{10}$$

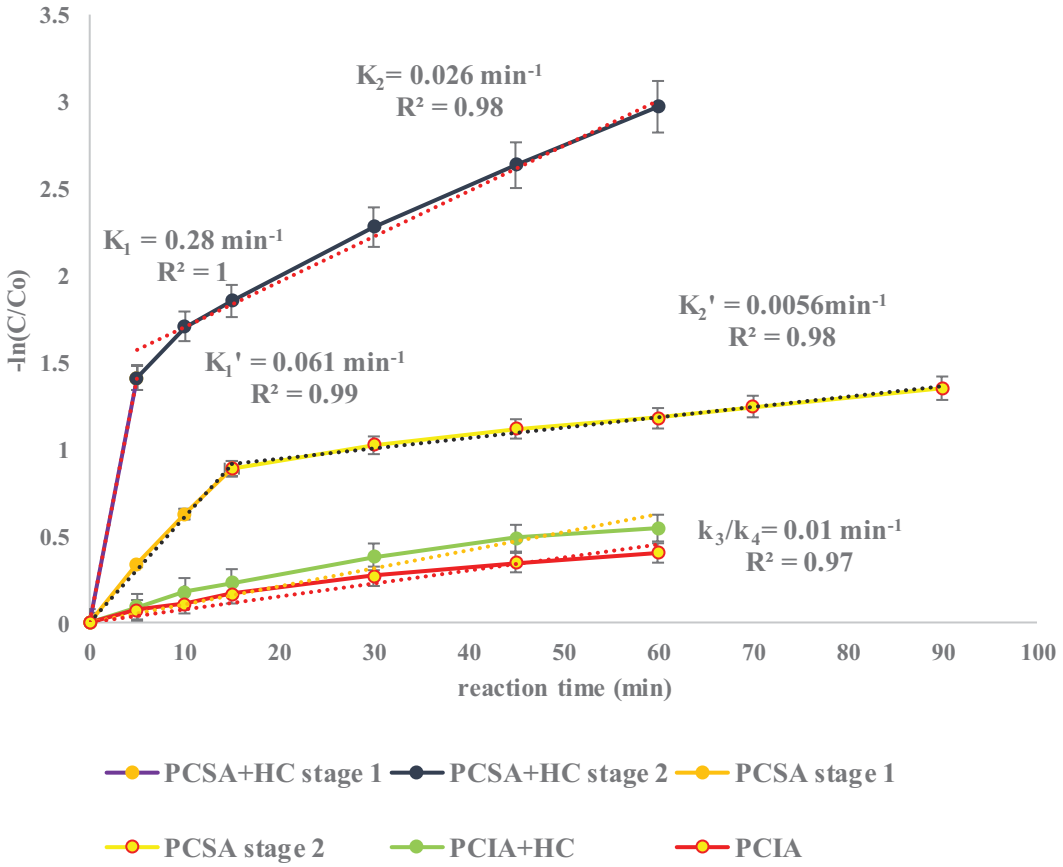

Fig. 12. Kinetics of different test conditions for CGTR.

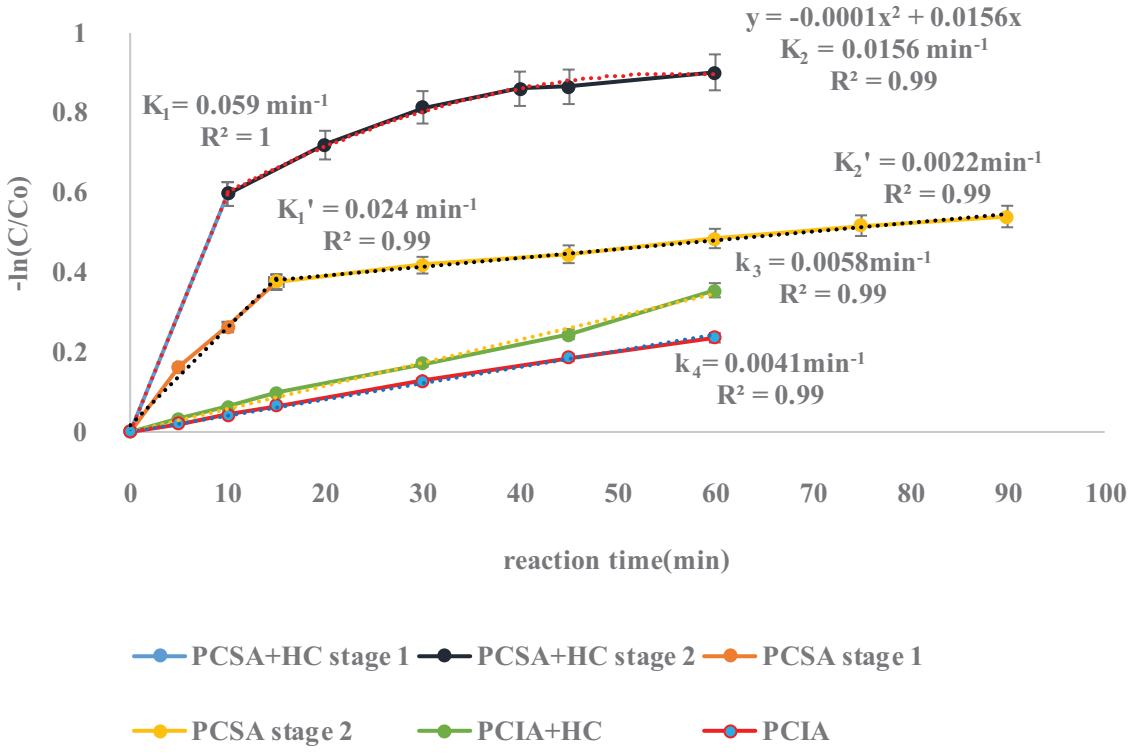

Fig. 13. Kinetics of different test conditions for STR.

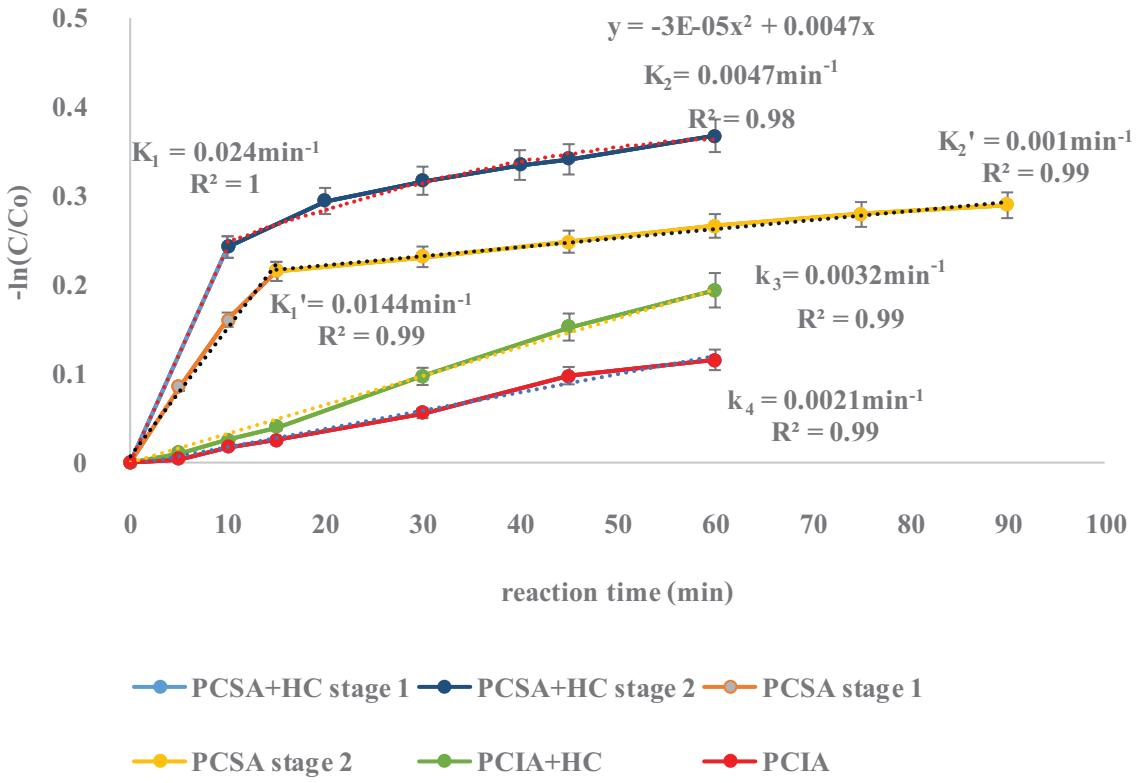

Fig. 14. Kinetics of different test conditions for CAR.

If coverage constant of water tends to unity due to its high concentration, then the equation gets simplified further as below equations [Eqs. (11)–(12)].

$$r = kC_{dye} \tag{11}$$

$$\frac{r(\text{PCSA})}{r(\text{PCIA})} = \frac{1}{K_{dye}} \tag{12}$$

Generally adsorption constant (K_{dye}) was noted to be less than unity [36]. Therefore it was inferred that rate of PCSA > rate of PCIA. The apparent reaction rate constant [Eq. (13)] was calculated assuming time-weighted average of K_1 (adsorption dominant kinetic constant) and K_2 (photocatalysis dominant kinetic constant).

$$k_{app} = \frac{K_1 t_1 + K_2 t_2}{t_1 + t_2} \tag{13}$$

In PCSA+HC and PCSA, initially the process was rapid and adsorption might be predominant. Later the process was gradual and photocatalysis might be predominant. The highest k_{app} (0.047 min^{-1}) was observed for CGTR (PCSA+HC). This may be attributed towards the micro-depth of the substrate [37,38] and synergism between adsorption, photocataysis and hydrodynamic cavitation [39].

The k_{app} for STR (PCSA+HC) was 0.49 times lesser than CGTR. The decrease in k_{app} might be due to the increase in effective substrate depth (3 cm). The k_{app} for CAR (PCSA+HC) was 0.17 times lesser than CGTR, where the effective substrate depth was 5.25 cm. This may be also due to further increase in substrate depth led to gradual decrease in incident photons throughout the reaction volume. The light photon penetration had a major influence in the reaction efficiency [40]. Further in case of PCSA+HC, hydrodynamic cavities were formed and subsequently collapsed in nanoseconds. This released high amount of energy, which caused water molecules to break into hydroxyl radicals or other oxidative radicals enhancing the mineralisation of dye molecules [9].

In the cases of PCSA, k_{app} was 0.015, 0.006 and 0.003 min^{-1} for CGTR, STR and CAR respectively. On average, k_{app} for PCSA was 0.3 times lesser than PCSA+HC. This may be due to the absence of hydrodynamic cavitation, leading to decrease in hydroxyl radical generation.

The K_3 (0.011 min^{-1}) and K_4 (0.01 min^{-1}) for PCIA+HC and PCIA in CGTR was same. But in the cases of STR and CAR, hydrodynamic cavities increased the reaction rate by 1.5 times. This indicates that the STR and CAR behaved like a continuous stirred tank reactor (CSTR) and not a Plug Flow reactor (PFR). In CSTR model, the system is perfectly mixed (the concentration inside the reactor is the same throughout the reactor). Instead in the PFR model, the concentration decreases along the flow without perfect mixing [41]. Even though the CSTR has higher mixing, yet poses various drawbacks such as less performance and less

energy efficiency. The absence of axial mixing in the PFR makes the reactor more effective than CSTR.

In a previous study consisting of Fenton-like oxidation of Crystal Violet dye, the CSTR showed 64.11% dye removal whereas PFR showed 98.88% in 15 min residence time [42]. In another study, fixed-bed reactor was operated in plug flow behaviour where 100% inactivation of *E. coli* was achieved [43].

The CGTR behaved as a plug flow reactor (PFR) which followed linear kinetic model. The similar kinetic analysis of hybrid processes for the removal of cephalexin antibiotic by ultrasonic/persulfate/nickel oxide nanoparticles followed the pseudo-first-order kinetics [44].

The PFR behaviour was mainly influenced by micro-depth longitudinal flow of CGTR [21]. On the other hand, in the case of STR and CAR, there was higher substrate depth or thickness, which induced higher mixing.

This CSTR flow regime of STR and CAR was validated by the second-order polynomial obtained in second-stage process of PCSA+HC. When using linear model the correlation coefficient was not near 1. Kinetic studies of adsorption and fenton-like process indicated that the best suitability of pseudo-second-order kinetic model was observed for the experimental data [45].

The following equations [Eqs. (14)–(17)] validated the second-order polynomial for continuous stirred tank reactor (CSTR), where k is the kinetic rate constant, C_o and C are the dye concentration at the start and at any time respectively.

$$\frac{C}{C_o} = \frac{1}{1+kt} \tag{14}$$

$$\ln\frac{C}{C_o} = -\ln\left(1+kt\right) \tag{15}$$

Expanding the power series for –ln(1 + kt),

$$-\ln\frac{C}{C_o} = kt - k^2\frac{t^2}{2} + k^3\frac{t^3}{3} \tag{16}$$

While $k < 1$, k^3, k^4, k^5…. tends to 0.

$$-\ln\frac{C}{C_o} = kt - k^2\frac{t^2}{2} \tag{17}$$

The second-order polynomial equation fitted well for STR and CAR. In the case of CGTR as PFR, the kinetics model obeyed linear dependence as below equation [Eqs. (18) and (19)].

$$\frac{C}{C_o} = e^{-kt} \tag{18}$$

$$-\ln\frac{C}{C_o} = kt \tag{19}$$

Table 3 shows the parameters [3,19,20,46] that were calculated for the three reactors: apparent kinetic constant (k_{app}), STY, PSTY, SRR, EEC, mmoles of organic carbon removed/kWh, mmoles of incident photons/kWh and photonic yield.

The STY is the m^3 throughput of wastewater treated per m^3 reactor per day for the conversion of 100 to 0.1 mM wastewater. The STY was calculated to be 32.65, 0.195, 0.019 $m^3/m^3/d$ for CGTR, STR and CAR respectively. The CGTR showed the highest STY among three reactors. Followed by STR which has the second highest STY, which was 167 times lesser than CGTR. The STY of CAR was the least, which was 10 times lesser than STR. The PSTY was the m^3 throughput of wastewater treated per m^3 reactor per day per kW for the conversion of 100 to 0.1 mM wastewater. The PSTY was calculated to be 1,360, 8, 0.8 $m^3/m^3/kW/d$ for CGTR, STR and CAR respectively. The CGTR showed the maximum PSTY so far achieved from our literature review [20]. This might be due to the highest photon utilization by the micro-depth fluid under recirculation of wastewater. The highest PSTY showed that the energy in terms of kilowatts was efficiently utilised for the dye removal. The SRR shows the specific removal of pollutant per amount of catalyst per hour of reaction time. The SRR was calculated as 4.74, 4.37, and 2.86 mg/g h for CGTR, STR and CAR respectively. The SRR was pollutant and catalyst specific. In all cases, the photocatalyst dosage used was 2 g/L. But the dye removal was 94.8%, 87.4% and 57.2% for CGTR, STR and CAR respectively for one hour of reaction time. Therefore this implied that highest amount of dye was removed in case of CGTR. EEC showed the electrical energy consumed per m^3 reactor for the specific log reduction of pollutant. The EEC was calculated to be 0.008, 0.01, 0.03 kWh/m^3 for CGTR, STR and CAR respectively. The electrical energy utilised was lowest in case of CGTR. In case of STR, the EEC was 1.25 times higher than CGTR.

Table 3
Comparative parameters for reactors and test conditions

Parameters	CGTR	STR	CAR
K_1, min^{-1}	0.28	0.059	0.024
K_2, min^{-1}	0.026	0.0156	0.0047
k_{app}*, min^{-1}	0.047	0.023	0.008
K_1', min^{-1}	0.061	0.024	0.014
K_2', min^{-1}	0.006	0.002	0.001
k_{app}, min^{-1}	0.015	0.006	0.003
K_3, min^{-1}	0.01	0.006	0.003
K_4, min^{-1}	0.01	0.004	0.002
STY, $m^3/m^3/d$	32.65	0.195	0.019
PSTY, $m^3/m^3/d/kW$	1360	8	0.8
SRR, mg/g h	4.74	4.37	2.86
EEC, kWh/m^3	0.008	0.01	0.03
mmoles of *C* removed/kWh, mmoles/kWh	8.33	5.73	3.96
mmoles of incident photons/kWh, mmoles/kWh	0.1	0.098	0.087
Photonic yield	5.64	5.172	3.963

Further in the case of CAR, the EEC was 3.75 times higher than that of CGTR. This implied that CGTR exhibited the maximum energy efficiency compared to the other reactors.

When calculating the mmoles of organic carbon removed/kWh, CGTR showed highest (8.33 mmoles/kWh) among the three reactors. Although the energy spent for all the reactors was 24 W (equivalent to 0.024 kWh) during the reaction, the mmoles of carbon removed/kWh for STR and CAR was 0.69 and 0.47 times lesser when compared to that of CGTR. This implied that maximum total organic carbon (TOC) was reduced for one kWh of energy spent in CGTR.

Ferrioxalate actinometrical experiments were carried out to determine the total amount of incident photons for the three reactors [3]. The intensity of colour represented in Fig. 15 implied the extent to which light photons were captured by potassium ferrioxalate resulting in oxidation. The absorbance difference was maximum for CGTR, which showed that this reactor configuration was energy efficient. The incident photons count was calculated to be as 6.74×10^{-10}, 6.58×10^{-10} and 5.77×10^{-10} moles/s. It was observed that for CGTR and STR had almost same incident photons count, due to the similar configuration of LEDs inside the outer vessel. In case of CAR, the incident photons were 0.85 times lesser than CGTR. The photonic yield was calculated by dividing the number of moles pollutant transformed and number of incident photons. The photonic yield was calculated to be 5.644, 5.172 and 3.963 for CGTR, STR and CAR respectively. Further, if we calculate the mmoles of photons incident per kWh, CGTR had the highest (0.1 mmoles incident photons/kWh) followed by STR (0.098 mmoles incident photons/kWh) and CAR (0.087 mmoles incident photons/kWh). This implied that CGTR and STR showed better incidence of light photons onto the substrate when compared to CAR. The exhaustive comparison of 8 parameters showed that CGTR was the most efficient in term of both performance and energy efficiency. Further it was inferred that micro-depth reactors could be a transitional design between classical annular reactors and advanced microreactors.

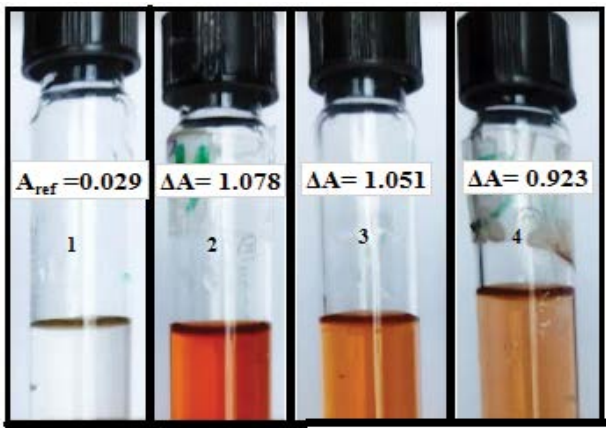

Fig. 15. Ferrioxalate solution after addition of 0.1% 1,10-phenanthroline (1. Reference, 2. CGTR, 3. STR, 4. CAR).

Table 4
Cost comparison of reactors

Cost component/reactor	CGTR	STR	CAR
Amortization costs	$/L of wastewater treated		
1. Stainless steel	30	20	20
2. Light source	195	195	40
3. Pump and piping systems	10	10	10
4. Glass tube	30	10	10
Total	265	235	80

3.3. Cost comparison of reactors

One of the major criteria important for building large scale photocatalytic reactor is cost. Total cost involves amortization cost, electricity cost, maintenance cost, labour cost etc. In general, around 60% of the total costs are influenced by amortization costs.

The following Table 4 shows the comparison of amortization costs for the three types of reactors. The electricity unit consumed for an hour was 0.024 kWh for the three reactors, which makes the operational cost quantitatively small. It was observed that for LED-based photocatalytic reactors (CGTR and STR), 70%–80% of total amortization cost was influenced by LEDs. In the case of conventional lamps-based photocatalytic reactor (CAR), the light source contributed around 50% of the total amortization cost.

Although the cost of UV-LEDs were higher than conventional lamps, there were no heating problems faced by LED-based photocatalytic reactors. In addition, the photon incident was higher in case of LED-based photocatalytic reactors (CGTR and STR) when compared to CAR. Therefore it was inferred that in building the large scale reactor, LED-based photocatalytic reactors would encounter lesser problems with respect to replacement of light source and heating of reactor when compared to conventional lamps-based photocatalytic reactor.

4. Conclusions

The study is about an exhaustive comparison between three photocatalytic reactors (CGTR, STR and CAR). The comparative parameters for performance and energy efficiency were calculated. The best parameter values were obtained for CGTR: apparent kinetic constant (0.047 min^{-1}), space time yield (32.65 $m^3/m^3/d$), photocatalytic space time yield (1,360 $m^3/m^3/d/kW$), specific removal rate (4.74 mg/g h), electrical energy consumption (0.008 kWh/m^3), 8.33 mmoles of organic carbon removed/kWh, 0.1 mmoles of incident photons/kWh and 5.64 photonic yield. The study concludes that micro-depth pollutant could be a transitional design for achieving the maximum performance and energy utilization.

5. Research suggestions

Future researchers could explore on various other designs for high-throughput microreactors. Also efforts could focus on demonstration of other novel suspended catalyst materials for the removal of other emerging contaminants in a combined/coupled advanced oxidation processes.

Acknowledgement

The authors would like to acknowledge the Department of Science and Technology, Government of India for funding the research under DST INSPIRE fellowship (INSPIRE Code IF180373).

References

[1] M.R. Samarghandi, A. Dargahi, A. Shabanloo, H.Z. Nasab, Y. Vaziri, A. Ansari, Electrochemical degradation of methylene blue dye using a graphite doped PbO_2 anode: optimization of operational parameters, degradation pathway and improving the biodegradability of textile wastewater, Arabian J. Chem., 13 (2020) 6847–6864.
[2] M.R. Samarghandi, A. Dargahi, H.Z. Nasab, E. Ghahramani, S. Salehi, Degradation of azo dye Acid Red 14 (AR14) from aqueous solution using H_2O_2/nZVI and $S_2O_8^{2-}$/nZVI processes in the presence of UV irradiation, Water Environ. Res., 92 (2020) 1173–1183.
[3] K.P. Sundar, S. Kanmani, Studies on the development of a novel UV-LED strip photocatalytic reactor and performance on dye decolourization, Environ. Prot. Eng., 47 (2021) 31–57.
[4] A. Hossain, A.B.M. Sadique Rayhan, M.J. Raihan, A. Nargis, I.M.I. Ismail, A. Habib, A.J. Mahmood, Kinetics of degradation of Eosin Y by one of the advanced oxidation processes (AOPs)–Fenton's process, Am. J. Anal. Chem., 7 (2016) 863–879.
[5] M. Afsharnia, M. Kianmehr, H. Biglari, A. Dargahi, A. Karimi, Disinfection of dairy wastewater effluent through solar photocatalysis processes, Water Sci. Eng., 11 (2018) 214–219.
[6] E. Asgari, B. Hashemzadeh, G. Hassani, M. Manshouri, A. Sheikhmohammadi, Y. Fakhri, Enhancement the BuP photocatalytic degradability by UVC/ZnO through adding exogenous oxidant: mechanism, kinetic, energy consumption, J. Environ. Chem. Eng., 8 (2020) 1–28.
[7] A. Almasi, A. Dargahi, M. Mohammadi, A. Azizi, A. Karami, F. Baniamerian, Z. Saeidimoghadam, Application of response surface methodology on cefixime removal from aqueous solutions by ultrasonic/photooxidation, Int. J. Pharm. Technol., 8 (2016) 16728–16736.
[8] V.K. Saharan, M.P. Badve, A.B. Pandit, Degradation of Reactive Red 120 dye using hydrodynamic cavitation, Chem. Eng. J., 178 (2011) 100–107.
[9] S.K. Gujar, P.R. Gogate, P. Kanthale, R. Pandey, S. Thakre, M. Agrawal, Combined oxidation processes based on ultrasound, hydrodynamic cavitation and chemical oxidants for treatment of real industrial wastewater from cellulosic fiber manufacturing sector, Sep. Purif. Technol., 257 (2021) 117888, doi: 10.1016/j.seppur.2020.117888.
[10] M.R. Samarghandi, A. Rahmani, G. Asgari, G. Ahmadidoost, A. Dargahi, Photocatalytic removal of cefazolin from aqueous solution by AC prepared from mango seed + ZnO under UV irradiation, Global NEST J., 20 (2018) 399–407.
[11] E. Asgari, A. Sheikhmohammadi, H. Nourmoradi, S. Nazari, M. Aghanaghad, Degradation of ciprofloxacin by photocatalytic ozonation process under irradiation with UVA: comparative study, performance and mechanism, Process Saf. Environ. Prot., 147 (2021) 356–366.
[12] B. Hashemzadeh, H. Alamgholiloo, N.N. Pesyan, E. Asgari, A.Sheikhmohammadi, J. Yeganeh, H. Hashemzadeh, Degradation of ciprofloxacin using hematite/MOF nanocomposite as a heterogeneous Fenton-like catalyst: a comparison of composite and core-shell structures, Chemosphere, 281 (2021) 130970, doi: 10.1016/j.chemosphere.2021.130970.
[13] K. Hasani, M. Moradi, S.A. Mokhtari, H. Sadeghi, A. Dargahi, M. Vosoughi, Degradation of basic violet 16 dye by electroactivated persulfate process from aqueous solutions and toxicity assessment using microorganisms: determination of by-products, reaction kinetic and optimization using Box–Behnken design, Int. J. Chem. Reactor Eng., 19 (2021) 261–275.
[14] S. Lettieri, M. Pavone, A. Fioravanti, L.S. Amato, P. Maddalena, Charge carrier processes and optical properties in TiO_2 and TiO_2-based heterojunction photocatalysts: a review, Materials, 14 (2021) 1–57.
[15] K.N. Ewelina, A. Wanag, K.K. Joanna, L. Kowalczyk, M. Zgrzebnicki, B. Tryba, J. Przepiórski, A.W. Morawski, Methylene blue decomposition on TiO_2/reduced graphene oxide hybrid photocatalysts obtained by a two-step hydrothermal and calcination synthesis, Catal. Today, 357 (2020) 630–637.
[16] S. Ren, P. Rong, Q. Yu, Preparations, properties and applications of graphene in functional devices: a concise review, Ceram. Int., 44 (2018) 11940–11955.
[17] T.F. Yeh, J. Cihlar, C.Y. Chang, C. Cheng, H. Teng, Roles of graphene oxide in photocatalytic water splitting, Mater. Today, 16 (2013) 78–84.
[18] A. Enesca, The influence of photocatalytic reactors design and operating parameters on the wastewater organic pollutants removal—a mini-review, Catalysts, 11 (2021) 1–22.
[19] M.S. Miguel, C. Pablos, R.V. Grieken, J. Marugan, Influence of light distribution on the performance of photocatalytic reactors: LED vs. mercury lamps, Appl. Catal., B, 215 (2017) 1–7.
[20] K.P. Sundar, S. Kanmani, Progression of photocatalytic reactors and it's comparison: a review, Chem. Eng. Res. Des., 154 (2020) 135–150.
[21] M. Enis Leblebici, B. Van den Bogaert, G.D. Stefanidis, T.V. Gerven, Efficiency vs. productivity in photoreactors, a case study on photochemical separation of Eu, Chem. Eng. J., 310 (2017) 240–248.
[22] A.N. Syahida, H. Sutanto, I. Alkian, F.D.D. Irianti, A.A. Wibowo, P. Priyono, Synthesized and characterization nanosized synthesis Fe_3O_4 powder from natural iron sand, J. Phys.: Conf. Ser., 1943 (2021) 012013.
[23] W.K. Jo, G.T. Park, R.J. Tayade, Synergetic effect of adsorption on degradation of malachite green dye under blue LED irradiation using spiral-shaped photocatalytic reactor, Chem. Technol. Biotechnol., 90 (2015) 2280–2289.
[24] R. Siburian, H. Sihotang, S.L. Raja, M. Supeno, C. Simanjuntak, New route to synthesize of graphene nano sheets, Orient. J. Chem., 34 (2018) 182–187.
[25] Q. Cheng, Y. Okamoto, N. Tamura, M. Tsuji, S. Maruyama, Y. Matsuo, Graphene-like-graphite as fast-chargeable and high-capacity anode materials for lithium ion batteries, Sci. Rep., 7 (2017) 1–14.
[26] L.P. Bakos, L. Sarvari, K. Laszlo, J. Mizsei, Z. Konya, G. Halasi, K. Hernadi, A. Szabo, D. Berkesi, I. Bakos, I.M. Szilagyi, Electric and photocatalytic properties of graphene oxide depending on the degree of its reduction, Nanomaterials, 10 (2020) 1–14.
[27] M. Acik, Y.J. Chabal, A review on thermal exfoliation of graphene oxide, J. Mater. Sci. Res., 2 (2013) 101–112.
[28] M. Ahn, R. Liu, C. Lee, W. Lee, Designing carbon/oxygen ratios of graphene oxide membranes for proton exchange membrane fuel cells, J. Nanomater., 10 (2019) 1–9.
[29] D.C. Marcano, D.V. Kosynkin, J.M. Berlin, A. Sinitskii, Z. Sun, A. Slesarev, L.B. Alemany, W. Lu, J.M. Tour, Improved synthesis of graphene oxide, ACS Nano, 4 (2010) 4806–4814.
[30] M. Kocijan, L. Curkovic, D. Ljubas, K. Muzina, I. Bacic, T. Radosevic, M. Podlogar, I. Bdikin, O.I. Gonzalo, M.J. Hortiguela, G. Goncalves, Graphene-based TiO_2 nanocomposite for photocatalytic degradation of dyes in aqueous solution under solar-like radiation, Appl. Sci., 11 (2021) 1–15.
[31] R.C. Pawar, V. Khare, C. Sunyong Lee, Hybrid photocatalysts using graphitic carbon nitride/cadmium sulfide/reduced graphene oxide (g-C_3N_4/CdS/RGO) for superior photodegradation of organic pollutants under UV and visible light, Dalton Trans., 43 (2014) 12514–12527.
[32] S.H.S. Chan, T.Y. Wu, J.C. Juan, C.Y. Teh, Recent developments of metal oxide semiconductors as photocatalysts in advanced oxidation processes (AOPs) for treatment of dye waste-water, J. Chem. Technol. Biotechnol., 86 (2011) 1130–1158.
[33] N.T. Padmanabhan, N. Thomas, J. Louis, D.T. Mathew, P. Ganguly, H. John, S.C. Pillai, Graphene coupled TiO_2 photocatalysts for environmental applications: a review, Chemosphere, 271 (2021) 129506, doi: 10.1016/j.chemosphere.2020.129506.
[34] A. Mahmood, X. Wang, X. Xie, J. Sun, Degradation behaviour of mixed and isolated aromatic ring containing VOCs:

Langmuir-Hinshelwood kinetics, photodegradation, in-situ FTIR and DFT studies, J. Environ. Chem. Eng., 9 (2021) 105069, doi: 10.1016/j.jece.2021.105069.
[35] P.S. Ghosal, A.K. Gupta, Development of a generalized adsorption isotherm model at solid-liquid interface: a novel approach, J. Mol. Liq., 240 (2017) 21–24.
[36] J.L. Luna, L.E.R. Montes, S.M. Vargas, A.I. Martínez, O.F.M. Ricardez, M.C.A.G. Chavez, R.C. Gonzalez, F.A.S. Dominguez, M.C.C. Diaz, V.V. Hipolito, Linear and nonlinear kinetic and isotherm adsorption models for arsenic removal by manganese ferrite nanoparticles, SN Appl. Sci., 1 (2019) 1–19.
[37] T. Claes, A. Dilissen, M.E. Leblebici, T.V. Gervena, Translucent packed bed structures for high throughput photocatalytic reactors, Chem. Eng. J., 361 (2019) 725–735.
[38] Z. Dong, Z. Wena, F. Zhao, S. Kuhn, T. Noel, Scale-up of micro- and milli-reactors: an overview of strategies, design principles and applications, Chem. Eng. Sci.: X, 10 (2021) 100097, doi: 10.1016/j.cesx.2021.100097.
[39] X. Wang, J. Jia, Y. Wang, Combination of photocatalysis with hydrodynamic cavitation for degradation of tetracycline, Chem. Eng. J., 315 (2017) 274–282.
[40] G. Meir, M.E. Leblebici, S. Fransen, S. Kuhn, T.V. Gerven, Principles of co-axial illumination for photochemical reactions: part 1. Model development, J. Adv. Manuf. Process., 2 (2020) 1–16.
[41] E. Colombo, M. Ashokkumar, Comparison of the photocatalytic efficiencies of continuous stirred tank reactor (CSTR) and batch systems using a dispersed micron sized photocatalyst, RSC Adv., 7 (2017) 48222–48229.
[42] M.M. Sara, F. Bahadori, M. Ghadiri, A. Afghan, Enhancing Fenton-like oxidation of crystal violet over Fe/ZSM-5 in a plug flow reactor, React. Kinet. Mech. Catal., 133 (2021) 1061–1073.
[43] I. Thakur, A. Verma, B. Ormeci, Visibly active Fe-TiO_2 composite: a stable and efficient catalyst for the catalytic disinfection of water using a once-through reactor, J. Environ. Chem. Eng., 9 (2021) 1–12.
[44] S.M. Abdolmotaleb, Z. Ghorbanian, G. Asgari, A. Dargahi, Degradation of CEX antibiotic from aqueous environment by US/$S_2O_8^{2-}$/NiO process: optimization using Taguchi method and kinetic studies, Desal. Water Treat., 171 (2019) 444–455.
[45] S. Afshin, Y. Rashtbari, M. Vosough, A. Dargahi, M. Fazlzadeh, A. Behzad, M. Yousefi, Application of Box–Behnken design for optimizing parameters of hexavalent chromium removal from aqueous solutions using Fe_3O_4 loaded on activated carbon prepared from alga: kinetics and equilibrium study, J. Water Process Eng., 42 (2021) 1–9.
[46] M.E. Leblebici, G.D. Stefanidis, T.V. Gerven, Comparison of photocatalytic space-time yields of 12 reactor designs for wastewater treatment, Chem. Eng. Process. Process Intensif., 97 (2015) 106–111.